Icarus 321 (2019) 1013–1025

Contents lists available at ScienceDirect

Icarus

journal homepage: www.elsevier.com/locate/icarus

A new hybrid framework for simulating hypervelocity asteroid impacts and gravitational reaccumulation

Charles El Mir[a], KT Ramesh[*,a,b,c], Derek C. Richardson[d]

[a] Department of Mechanical Engineering, The Johns Hopkins University, Baltimore, MD 21218, USA
[b] Department of Earth and Planetary Sciences, The Johns Hopkins University, Baltimore, MD 21218, USA
[c] Hopkins Extreme Materials Institute, The Johns Hopkins University, Baltimore, MD 21218, USA
[d] Department of Astronomy, University of Maryland, College Park, MD 20742, USA

ARTICLE INFO

Keywords:
Impact processes
Collisional physics
Asteroids
Dynamics

ABSTRACT

We present a hybrid approach for simulating hypervelocity impacts onto asteroids. The overall system response is separated into two stages based on their different characteristic timescales. First, the short-timescale fragmentation phase is simulated using a modified version of the Tonge–Ramesh material model implemented in a Material Point Method framework. Then, a consistent hand-off to an *N*-body gravity code is formulated to execute the long-timescale gravitational reaccumulation calculation. We demonstrate this hybrid approach by considering the 5 km/s head-on impact of a 1.21 km diameter basalt impactor on a 25 km diameter target asteroid. The impact event resulted in the fragmentation, but not complete disruption, of the entire target. A granular core is observed at the end of the fragmentation simulations, which acts as a gravity well over which reaccumulation occurs in the *N*-body simulations. Our results suggest that disruption thresholds for rocky asteroids are higher when energy-dissipating mechanisms such as granular flow and pore collapse are included.

1. Introduction

Asteroid impacts ranging from small-scale cratering events to catastrophic disruption have played a crucial role in the evolution of the asteroid belt. Studying the impact history of asteroids also provides a glimpse into the active processes from the early formation of the solar system. Detailed information about asteroid shapes, composition, and orbital dynamics has been collected through remote sensing (Hérique et al., 2017) and spacecraft missions (Barucci et al., 2011); however, the internal structure of those asteroids remains poorly constrained. Is an asteroid a fractured monolith, or a rubble pile of gravitationally bound fragments? This distinction is difficult to make even for asteroids with known bulk densities. As pointed out in Asphaug (2009), the same data for asteroid 433 Eros could be interpreted to support a monolithic structure with impact-induced grooves (Prockter et al., 2002), or to support a rubble pile (Asphaug et al., 2002). Since laboratory experiments alone can not sufficiently reproduce the scales and conditions within asteroid impacts, numerical modeling has become a valuable approach for providing insight into the internal structure of asteroids, asteroid surface modification, and the formation of asteroid families and satellites.

Studies of asteroid hazard mitigation, together with the prospect of kinetic impactor-based space experiments such as the DART mission (Cheng et al., 2015), also call for detailed computational modeling of hypervelocity impacts onto small (sub-km) asteroids. A primary result of interest in asteroid mitigation studies is a measure of the momentum transfer characterized by the momentum enhancement factor, β (Lawrence, 1990; Walker and Chocron, 2011). The β-factor is the ratio of the total momentum imparted to the post-impact target and the initial momentum of the impactor. If no material is ejected, then only the momentum of the impactor has been added to the target and $\beta = 1$. If material is ejected from the target, this can enhance the momentum transfer to the body ($\beta > 1$). As such, tracking the fate of ejecta from fragmentation to ejection and reaccumulation is crucial in capturing the momentum enhancement of the target following a high speed impact.

Numerous studies have demonstrated the importance of multi-stage modeling of asteroid impact processes so as to follow the ejecta from the early stages of impact to the late stage of gravitational reaccumulation (e.g. Michel et al., 2001; Durda et al., 2004, 2007). Michel et al. (2001) simulated the catastrophic disruption of a large parent asteroid and the subsequent formation of asteroid satellites using a two-step process where material fragmentation during the first few seconds was captured using a Smoothed Particle Hydrodynamics (SPH) code. In their simulations, the target was fully disrupted at the end of

* Corresponding author at: Hopkins Extreme Materials Institute, The Johns Hopkins University, Baltimore, MD 21218, USA.
E-mail address: ramesh@jhu.edu (K. Ramesh).

https://doi.org/10.1016/j.icarus.2018.12.032
Received 22 May 2018; Received in revised form 10 December 2018; Accepted 13 December 2018
Available online 19 December 2018
0019-1035/

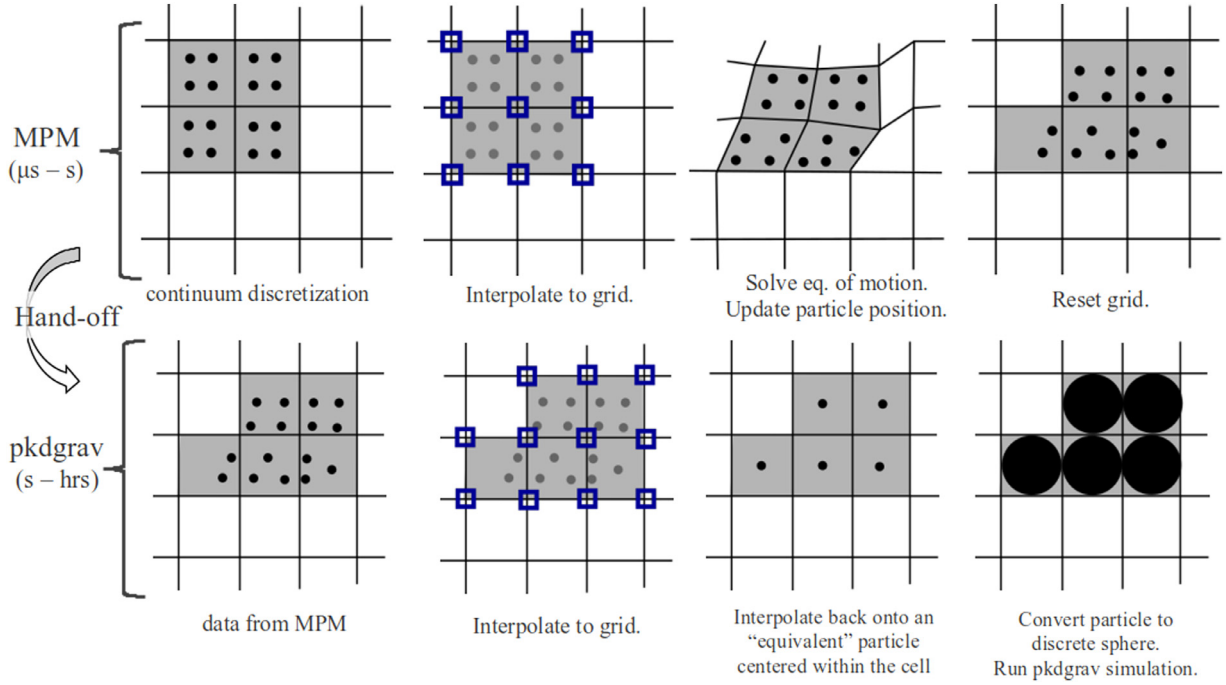

Fig. 1. The top row illustrates the particle/grid interpolations performed during an MPM timestep. A continuum is discretized into a set of material points where all state variables are stored. At the beginning of a timestep, mass and velocity at grid nodes are calculated by interpolating the values at the material points. The equations of motion are solved on the grid, and the displacements are interpolated back to the material points. The background grid is discarded and reset at the end of the timestep. The bottom row illustrates our MPM-to-`pkdgrav` hand-off method that is consistent with the MPM interpolations. This hand-off procedure is discussed in Section 4.2.

the SPH calculation. The smoothed particles in SPH were then transformed into discrete rigid spheres, and their positions and velocities handed off to a gravitational *N*-body code (`pkdgrav`) to trace the evolution of the system over several days post-impact. Since particles in SPH do not have a physical radius, and owing to the smoothing kernel in SPH codes, an iterative approach is often employed in which the particles' radii are sequentially reduced until there is no overlap among the spheres.

The feasibility of this two-step approach was demonstrated through a detailed parametric study (Michel et al., 2002) and was later used to explore the origin of asteroid families and satellites (Michel et al., 2003; Durda et al., 2004, 2007). The approach also suggested a possible origin of asteroid (25143) Itokawa as a rubble-pile aggregate by-product of a catastrophic disruption event (Richardson et al., 2009; Michel and Richardson, 2013). It is notable that in all of these studies, the initial impact leads to the complete disruption of the target asteroid, down to the SPH numerical resolution, and the number of fragments was therefore equal to the number of SPH particles. This total disruption outcome was insensitive to the chosen resolution, leaving no individual fragment larger than the particle discretization size at the end of the fragmentation phase (Michel et al., 2002).

Recently, Tonge et al. (2016) investigated the impact history of asteroid (433) Eros using a new material model for brittle materials and a very different numerical approach. The Tonge–Ramesh material model incorporates multiple physical processes that occur during an impact event, such as dynamic crack propagation and damage accumulation, porosity growth and pore compaction, and granular flow of highly damaged materials. Tonge et al. (2016) simulated the formation of the largest craters on Eros (Himeros, Psyche, and Shoemaker) through sequential impact events onto an assumed shape model of a "young" monolithic Eros. Interestingly, their results showed the shattering but not complete disruption of the target throughout all of the three impact events. In addition, a final porosity of 20% was predicted within Eros as a result of the granular flow of the fragmented material. This porosity level is not far from the current observed bulk porosity of about 25% and suggests that Eros could be heavily fractured rather than a rubble pile aggregate that reaccumulated following a catastrophic disruption (Wilkison et al., 2002). However, the Tonge et al. (2016) results focused on the short-timescale fragmentation phase and did not account for long-term gravity effects such as reaccumulation of material or the target's compaction due to self-gravity.

In this work, we follow the hybrid technique of Michel et al. (2001) by separating the impact event into two main timescales: the short-timescale fragmentation phase, and the long-timescale gravitational phase. We use a modified version of the Tonge–Ramesh model that incorporates the Tillotson equation of state and is implemented in a Material Point Method (MPM) framework. We validate the material model by comparing the predicted dynamic tensile strengths with Brazilian disk experiments on basalt. We use the validated model to first simulate the fragmentation phase, which is dominated by the stress waves traveling through the target. Then, a suitable cut-off time is selected to hand off the simulation to the *N*-body code `pkdgrav` for the long-timescale gravitational phase. Unlike SPH-based hand-offs, the conversion from particles to discrete spheres is greatly facilitated by taking advantage of the Eulerian-Lagrangian nature of MPM. We implement this approach to study the collisional outcome of a 1.21 km impactor onto a 25 km target (as in the Michel and Richardson, 2013, paper) at the early stages and then hand off to the *N*-body gravity code, `pkdgrav`, for the long-timescale gravity evolution.

2. Numerical modeling

2.1. The material point method

The Material Point Method (MPM) is an extension of the particle-in-cell (PIC) method in which a continuum body is discretized into a set of Lagrangian material points (or particles) moving within a background grid (Brackbill and Ruppel, 1986; Brackbill et al., 1988; Sulsky et al., 1994, 1995). State variables are stored at the material points, while the computational grid is used to calculate the necessary gradients for

solving the equations of motion. This background grid is discarded and reset after each timestep, avoiding the undesirable mesh tangling and advection errors of mesh-based methods when modeling large deformations (Fig. 1, top row). This dual particle-grid nature defines two numerical resolutions related to (a) the cell size or spacing, and (b) the number of particles per cell. In effect, the cell spacing defines the smallest lengthscale for which a particular gradient can be calculated, and the number of particles per cell determines the integration order within each cell. One of the advantages of MPM is that the use of the grid renders it trivial to apply boundary conditions and resolve material contacts. The numerical difficulties in SPH related to surface particles (when the kernel support is not fully included) or the tensile instability (Swegle et al., 1995) (from kernel approximation) are therefore eliminated in MPM. In addition, contacts are resolved trivially in MPM by means of the background grid, eliminating the need for the expensive neighbor-search algorithm in SPH when boundary conditions are not contained in the weak form of the conservation equations (Kupchella et al., 2015).

As such, MPM is well suited for simulating large deformations of solids and has been used in a number of applications including modeling injury in soft biological tissues (Ionescu et al., 2006; Ganpule et al., 2017), response of granular materials (Bardenhagen et al., 2000a,b, 2001), and asteroid impacts (Tonge et al., 2016).

In MPM, a body is first discretized into a set of material points at which all variables (mass, velocity, temperature, ...) are stored. An integration for a timestep Δt starting at a time t begins by interpolating the material point mass m_p and momentum $\boldsymbol{p}_p^t$ onto the grid such that the total nodal mass m_n and nodal momentum $\boldsymbol{p}_n^{t_0}$ are conserved. The nodal mass is obtained by interpolating the contributions from surrounding material points using a shape function $S_{np} = S_n(\boldsymbol{x}_p)$ as:

$$m_n = \sum_p S_{np} m_p \tag{1}$$

$$\boldsymbol{p}_n^t = \sum_p S_{np} \boldsymbol{p}_p^t \tag{2}$$

The grid mass matrix is constant throughout a single timestep, but is not necessarily the same at a subsequent timestep. Since material points can move across cell boundaries, the individual components of the grid mass matrix could change and should be computed at the beginning of every timestep. Consequently, a lumped mass matrix is generally preferred in order to minimize the computational cost related to matrix inversion at each timestep. Following Eq. (2), momentum is conserved by construction.

The grid velocities can then be calculated by dividing the nodal momentum by the nodal mass:

$$\boldsymbol{v}_n^t = \boldsymbol{p}_n^t / m_n \tag{3}$$

After solving on the grid the weak form of the potential energy minimization, the nodal velocities at the end of the timestep are incremented as:

$$\boldsymbol{v}_n^{t+\Delta t} = \boldsymbol{v}_n + \boldsymbol{a}_n \Delta t, \tag{4}$$

where $\boldsymbol{a}_n$ is the nodal acceleration.

The material point positions and velocities are then updated by interpolating the velocities and accelerations from the grid nodes:

$$\boldsymbol{x}_p^{t+\Delta t} = \boldsymbol{x}_p^t + \sum_n S_{np} \boldsymbol{v}_n^{t+\Delta t} \Delta t \tag{5}$$

$$\boldsymbol{v}_p^{t+\Delta t} = \boldsymbol{v}_p^t + \sum_n S_{np} \boldsymbol{a}_n \Delta t \tag{6}$$

Note that Eqs. (1) and (2) are particle-to-grid interpolations whereas Eqs. (5) and (6) are grid-to-particle interpolations.

Finally, the material point strains and Cauchy stresses are incremented using the strain rate tensor, which is the symmetric part of the velocity gradient.

$$\Delta \boldsymbol{\epsilon}_p^{t+\Delta t} = \boldsymbol{E}_p \Delta t = \frac{1}{2} \sum_n (\nabla S_{np} \boldsymbol{v}_n^{t+\Delta t} + \boldsymbol{v}_n^{t+\Delta t} \nabla S_{np}) \Delta t \tag{7}$$

The choice of functional expressions for evaluating the shape functions $S_n(\boldsymbol{x}_p)$ has direct consequences on the stability and convergence of MPM algorithms. The classical MPM approach assumed that the entire mass associated with a material point is concentrated at the location of that point, and as such the same shape functions from finite element (FEM) codes could be directly used, i.e, $S_{np} = N_{np} = N_n(\boldsymbol{x}_p)$ (Sulsky et al., 1994). Bardenhagen and Kober (2004) showed that this assumption leads to cell-crossing artifacts in which artificial internal forces are developed as a result of a particle crossing a cell boundary, and proposed instead a generalized form for the shape functions given by:

$$S_{np} = \frac{\int_{\Omega_p} \chi(\boldsymbol{x}_p) N_{np}(\boldsymbol{x}_p) \mathrm{d}\Omega}{\int_{\Omega_p} \chi(\boldsymbol{x}_p) \mathrm{d}\Omega}, \tag{8}$$

where the material point $\boldsymbol{x}_p$ is assumed to occupy a domain Ω_p. If the material point occupies an infinitesimally small domain (a true point), then $\chi(\boldsymbol{x}_p)$ is a Dirac delta function, and the classical MPM formulation is recovered. Otherwise, if the material point is assumed to occupy a finite domain (i.e., $\chi(\boldsymbol{x}_p) = 1$ in some particle domain Ω_p and 0 elsewhere), then $\chi(\boldsymbol{x}_p)$ is a Heaviside step function. A number of alternative MPM shape function formulations such as the Undeformed Generalized Interpolation Material Point (UGIMP), the Convected Particle GIMP (CPGIMP), the Convected Particle Domain Integration (CPDI), and the second order CPDI (CPDI2) are then derived, all of which resolve the cell crossing issues of classical MPM. The particle domain Ω_p is typically rectangular (in 2D) prior to deformation. In UGIMP, these domains are assumed to be unchanged throughout the deformation, whereas in CPGIMP the area can deform while keeping its rectangular shape (i.e. stretched). On the other hand, CPDI and CPDI2 convect the initially rectangular particle domains into parallelograms or general quadrilaterals, respectively. The concept is similarly applied to general 3D shapes, and the particular details of the different functional expressions for $\chi(\boldsymbol{x}_p)$ are well discussed in Sadeghirad et al. (2011). In this work, we use a UGIMP interpolator. We note that UGIMP suffers from the so-called “numerical fracture”, which occurs when material points become separated by more than 1 cell and can no longer “communicate” through the background grid. This numerical anomaly is similar to the case of two SPH particles being separated by a distance larger than their radii of influence. The effects of this numerical fracture can be severe when modeling a material that can sustain very large deformations without fracturing (such as polymers), but is minimal for brittle materials simulated at high-enough resolutions. For the material and resolution used in this work, a separation of more than one numerical cell would only occur in the material points representing heavily fragmented blocks that are ejected from the impact crater, as will be demonstrated in Section 4.1, and the use of UGIMP is therefore acceptable.

In this work, we use the Uintah framework[1] (Germain et al., 2000; Guilkey et al., 2009) implementation of the MPM algorithm. Uintah is a highly parallel and adaptive computational tool equipped to tackle large-scale multi-physics problems spanning a wide range of length and time scales.

2.2. The Tonge–Ramesh material model for geomaterials

The internal strength of a rocky asteroid has a great effect on its collisional evolution. Following an impact onto brittle materials (such as rocks), stress waves travel through the target and probe the internal

[1] http://www.sci.utah.edu/download/uintah/.

structure causing the nucleation of cracks and propagation of pre-existing flaws. Several key mechanisms should be considered in this regime, including: (a)the thermodynamic response, described by both the elastic response and an appropriate equation of state; (b) the fragmentation response, described by the damage kinetics and interaction and growth of cracks; and (c) the motion of fragmented material, described by granular flow, pore compaction, and tensile fragmentation.

The Tonge–Ramesh material model (Tonge and Ramesh, 2016), which is now available in the public domain and has an implementation in the Uintah framework, is a mechanism-based material model for the high-strain-rate response of brittle materials that incorporates self-consistent dynamically interacting crack distributions, granular flow, and pore compaction. The material model was first used at the larger asteroid scales to demonstrate the impact-induced lineament formation and porosity growth on Eros (Tonge et al., 2016).

In this model, a brittle material is considered as a continuum with a spatial distribution of flaws that are smaller than the numerical resolution of the discretized body. The number density of flaws in a given representative volume is described by a scalar damage parameter, D, which characterizes the deterioration in elastic moduli. The material is considered granular once a critical damage level is reached, at which point it follows a granular flow yield surface.

The flaw distribution is discretized into N "bins" of similar flaw families, where the kth family with number density ω_k represents flaws with an initial size of s_k from which cracks of length l_k may be nucleated due to the imposed loading conditions. As such, the damage within a given material point is defined as:

$$D = \sum_{k=1}^{N_{bins}} \omega_k (s_k + l_k)^3 \tag{9}$$

In this work, we use a bounded Pareto distribution for the flaw density whose probability density function (PDF) is given by:

$$g(s) = \frac{\gamma s_{\min}^{\gamma} s^{-\gamma+1}}{1 - \left(\frac{s_{\min}}{s_{\max}}\right)^{\gamma}} \tag{10}$$

where s is the flaw size, γ the slope of the distribution, and $s_{\min}$ and $s_{\max}$ are the minimum and maximum resolved flaws within each computational cell, respectively. The values used in this work are given in Table 1. The microstructure is then simulated by generating the local flaw distribution at every particle, following a discretization algorithm that takes the computational discretization and the global flaw distribution as an input and computes a specific realization of the distribution of flaws within the sample volume. The discretization procedure is described in detail in Tonge and Ramesh (2016).

A self-consistent approach is used at each timestep to calculate the stress intensity factor resulting from the load as well as the crack environment. The crack growth rate ($\dot{l}$) is expressed as a function of the mode-I stress intensity factor K_I at the crack tip as:

$$\dot{l} = \frac{C_R}{\alpha_c}\left(\frac{K_I - K_{IC}}{K_I - 0.5K_{IC}}\right)^{\gamma_c}, \tag{11}$$

where K_{IC} is the critical stress intensity factor and C_R is the Rayleigh wave speed in the undamaged material. α_c and γ_c are non-dimensional parameters that determine the maximum crack speed, and how fast cracks approach that limiting speed with increasing K_I, respectively (Paliwal and Ramesh, 2008). Note that K_I must exceed K_{IC} for any crack growth to occur. The crack growth rate parameters are measured independently, with the crack speeds measured directly during dynamic failure using high-speed photography (Tonge et al., 2013). It follows that rate effects (Kimberley and Ramesh, 2011; Kimberley et al., 2013) become an inherent result of the interaction and growth of microcracks that have a finite propagation speed. In the Tonge–Ramesh material model, the nature of the rate sensitivity comes from a competition between the stress required to drive the activated cracks faster and the activation of the next set of available flaws. This interplay between local sampling, strain rate sensitivity, and specimen size is resolved for each flaw family at each material point. When the modeled geometry is larger, more realizations of the bigger flaws will be present in the local flaw distribution (compared to a smaller geometry of the same material), and lower stresses would be required (at the same strain rate) to initiate damage in the material by the initial activation of the largest flaw. The size dependence of strength and the transition strain rate then becomes a consequence of the different flaw distributions in the material points of different sizes.

As cracks propagate and damage evolves, the material reaches a critical damage level at which most microcracks have intersected and created many small fragments of material. Thereafter, the material is considered to be granular, and granular flow is activated. The current model considers a critical level of damage of $D = 0.125$ for the onset of

Table 1
Material model parameters used in this work.

EOS	ρ_0	2700 kg/m^3 m/s	
	A	2.67 $\times 10^{10}$ J/m^3	
	B	2.67 $\times 10^{10}$ J/m^3	Benz and Asphaug (1999)
	a	0.50	
	b	1.50	
	e_0	4.87 $\times 10^{8}$ J/kg	
Small-scale flaw distribution	Minimum Flaw size ($s_{\min}$)	5 μm	Tonge et al. (2016)
	Maximum Flaw size ($s_{\max}$)	1 mm	Tonge et al. (2016)
	Distribution Exponent (γ)	3.0	Housen and Holsapple (1999)
	Flaw Density (η)	2×10^{12} m^{-3}	Tonge et al. (2016)
	Number of flaw families (N_{bins})	25	
Large-scale flaw distribution	Minimum Flaw size ($s_{\min}$)	1.0 cm	
	Maximum Flaw size ($s_{\max}$)	80 m	
	Distribution Exponent (γ)	3.0	Housen and Holsapple (1999)
	Flaw Density (η)	250 m^{-3}	
	Number of flaw families (N_{bins})	25	
Micromechanics	Fracture Toughness (K_{IC})	1.6 MPa$\sqrt{\text{m}}$	Balme et al. (2004)
	Maximum Crack Velocity	0.2 C_r	Tonge et al. (2016)
	Crack Growth Exponent (γ_c)	1.0	
Granular flow	Slope of granular flow surface (A_{DP})	0.6	Martin et al. (2013)
	Damage Cohesive Strength (B_{DP})	0.3 MPa	
	Damage for Granular flow (D_c)	0.125	Tonge et al. (2016)
	Maximum Damage ($D_{\max}$)	0.2	
Pore compaction	Reference crush pressure (P_0)	75 MPa	
	Reference distension (α_0)	1.25	Fit to Jutzi et al. (2008)
	Consolidation pressure (P_c)	200 MPa	

granular flow, corresponding to when the flaws have grown so that their size is on average equal to half of the average spacing between flaws. Damage can keep evolving until the crack sizes become equal to the average spacing between flaws, at which point no further cracking of the grains is possible. Extensions of this crack coalescence model have been developed by Huq et al. (2016), but we do not use them in this work.

Once granular flow begins, we use a Drucker–Prager yield surface for granular plasticity defined as:

$$f(\boldsymbol{\sigma}) = \sqrt{\boldsymbol{s}:\boldsymbol{s}} + A_{DP}\left(\frac{\mathrm{tr}(\boldsymbol{\sigma})}{\sqrt{3}} - B_{DP}\right), \tag{12}$$

where $\boldsymbol{s}$ is the deviatoric part of the Cauchy stress tensor $\boldsymbol{\sigma}$, with $\boldsymbol{s} = \boldsymbol{\sigma} - \mathrm{tr}(\boldsymbol{\sigma})/3\ \boldsymbol{I}$ and $\boldsymbol{I}$ the identity tensor. A_{DP} is a positive parameter that controls the influence of the pressure on the yield limit and is related to the angle of friction used in a Mohr–Coulomb yield surface, while B_{DP} is the gravitational overburden pressure.

Porosity evolution is handled through a $P-\alpha$ porosity model, which relates the pressure P to the distention α and defines an additional yield surface as:

$$f_p(P,\alpha) = \begin{cases} \dfrac{P}{P_c - P_0} - \dfrac{P_0}{P_c - P_0}\exp\left(-\dfrac{P_c - P_0}{2P_0(\alpha-1)}(\alpha-\alpha_0)\right) & P < P_0 \\ (\alpha-1) - (\alpha_0-1)\alpha^2\left(\dfrac{P_c - P}{P_c - P_0}\right)^2 & P \le P < P_c \\ \alpha - 1 & P > P_c, \end{cases} \tag{13}$$

where $\alpha = \rho_s/\rho$ is the distention defined as the ratio of the solid's density ρ_s to the total density ρ, and $J = \alpha\rho_0/\rho_s = \rho_0/\rho$ is the volume change ratio. P_0 and α_0 are reference pressures and distentions respectively, and P_c is the consolidation pressure. For this work, these parameters are fit to experimental crush curves for pumice (Jutzi et al., 2009). Together, the P-α and the Drucker–Prager models define the shape of the yield surface where plastic behavior occurs. The elastic unloading is described by the damaged elastic moduli.

2.3. Equation of state

The pressure at a material point is obtained from the equation of state (EOS). Here, we implement a Tillotson EOS (Tillotson, 1962), which can be regarded as a generalized form of the Mie-Grüneisen EOS that was used in the original Tonge–Ramesh model. In the Tillotson EOS, the equivalent Grüneisen parameter (Γ) is a function of both density and specific internal energy, as opposed to being only a function of density in the classical Mie-Grüneisen EOS. We only consider the "solid" part of the Tillotson EOS and do not account for any phase transformations into liquid or vapor states, a limitation reasonable for the range of impact speeds that we consider. As such, the pressure of an undamaged solid is given by:

$$P(\mu,\eta,e) = \left[a + \frac{b}{e/(e_0/\eta^2)+1}\right]\rho_0\eta + A\mu + B\mu^2, \tag{14}$$

where a, b, A, B, e_0 are material-dependent Tillotson parameters, $\eta = J^{-1}$, and $\mu = \eta - 1$. The specific internal energy, e, contains contributions from the solid at zero-Kelvin (or a "cold" reference state) in addition to a thermal contribution. We use the material parameters outlined in Benz and Asphaug (1999), which are based on lunar gabbroic anorthosite (O'Keefe and Ahrens, 1982) parameters after substituting the basalt reference density and bulk modulus as reported by Nakamura and Fujiwara (1991). Damage evolution leads to a deterioration of the elastic modulii, following the relations derived in Tonge and Ramesh (2016). The effect of damage on the volumetric response is then accounted for by scaling the computed pressure for the undamaged material by the ratio of the damaged bulk modulus to the undamaged bulk modulus.

3. Experimental validation of the material model

3.1. Background

A number of numerical codes used in similar planetary-scale impact applications (Michel et al., 2002; Jutzi et al., 2008, 2010) incorporate the tensile brittle failure of Grady and Kipp (1980) as initially introduced into SPH by Benz and Asphaug (1994, 1995). In such models, the active number, n, of flaws is assumed ad hoc to be a function of strain ϵ through a power-law: $n(\epsilon) = k\epsilon^m$, where k and m are *so-called* material-dependent Weibull parameters.

Vardar and Finnie (1977) estimated a value of $m = 2.9$ for basalt, based on pulsed electron beam experiments. Melosh et al. (1992) derived a relationship between the rate-dependent tensile strength and the m parameter. Using the strain rate sensitivity reported in Grady and Lipkin (1980) ($\sigma_c \sim \dot{\epsilon}^{1/3} - \dot{\epsilon}^{1/4}$), they calculated m = 6–9. Their hydrocode simulations of impact experiments (Nakamura and Fujiwara, 1991) using $m = 9.5$ produced fits to fragment mass distributions. Benz and Asphaug (1994) performed numerical simulations of the same Nakamura and Fujiwara (1991) experiments using $m = 8.5$ and reproduced comparable masses and velocities for the largest fragment, but underestimated the masses of the smaller fragments. Note that such a process of varying m to match fragment statistics from experiments calibrates the simulations as opposed to specifically validating the material model, since different computational schemes (with the same material model) will predict different degrees of fracture and fragmentation (see the Sandia Fracture Challenge; Boyce et al. (2014)). Asphaug et al. (2002) reports a value of $m = 9.5$, derived indirectly from experimental measurements of tensile strength as a function of strain rate (Lindholm et al., 1974) .

However, Nakamura et al. (2007) performed a series of dynamic tensile experiments on the same basalt of Nakamura and Fujiwara (1991), following the method proposed by Weibull (1939, 1951) and demonstrated that the Weibull modulus m for their basalt should instead be in the range of $15-17$. Further, Nakamura et al. (2007) shows that $m = 17$ for a loading rate of 0.035 mm/min and $m = 39$ for a 14 mm/min loading. These experiments were effectively in the low strain rate regime with respect to the asteroid-scale impacts, where tensile stress is nearly constant, resulting in an m that tends to infinity (see Melosh et al., 1992, for the relationship between m and the strain rate). However, the approach has been used with fixed m to simulate dynamic events in planetary science for many years. This demonstrates the importance of distinguishing between (a) the calibration and validation of a material model, and (b) the "validation" of a simulation approach that incorporates an otherwise unvalidated material model. The fact than an inaccurate material model embedded in an impact simulation can capture some features of an impact experiment does not necessarily validate the combination of model plus computational approach. Of course, lacking primary laboratory data on material behavior, one does the best one can with the available data.

Our material model makes no assumption on the relationship between activated flaws and strain, nor on a direct dependence of strain rate and fracture strength. Instead, flaw activation and growth are based on a sub-scale fracture mechanics approach that relates the effective stress intensity factor (K_I) to crack growth using Eq. (11). The initial flaw distribution itself was calibrated using independent dynamic compression and edge-on ball impact experiments (Tonge and Ramesh, 2016). Here, we validate the model using a set of dynamic Brazilian disk experiments published by Ramesh et al. (2017) and demonstrate the model's ability to capture dynamic tensile failure over a wide range of strain rates. The material parameters used in our model are shown in Table 1.

3.2. Brazilian disk experiments

The Brazilian disk test is an experimental technique to indirectly measure the tensile strength of brittle materials (e.g. Zhao and Li (2000); Li and Wong (2013)) in which a thin circular disk is diametrically compressed until failure. The compression along one direction induces tensile stresses along the perpendicular direction. From the measured dynamic load-to-failure (F) for a disk with diameter D and thickness t, the tensile strength (σ_t) is defined as:

$$\sigma_t = \frac{2F}{\pi D t}. \tag{15}$$

Ramesh et al. (2017) present dynamic strength measurements for basalt with the dynamic load applied on the sample (10 mm in diameter and 2 mm thick) using a conventional Kolsky bar setup (Ramesh, 2009). A copper cushion is placed at the tungsten carbide platen/basalt sample interface to prevent stress concentrations at those surfaces. The experiments were carried out at strain rates ranging between $20 - 200\ s^{-1}$.

To validate the tensile failure in our material model, we set up the simulations with the same specimen geometry and use the velocity measurements recorded at the input bar as initial conditions. We discretize the sample using a numerical resolution that gives a cell spacing of 0.1 mm with one particle per cell. We assume an inverse power-law distribution of flaws that is characterized by a bounded Pareto distribution with a slope of 3.0. This slope gives self-similar scaling in the crack sizes where the average distance between flaws longer than a specified size scales linearly with the crack length and is consistent with the experimental observations of Housen and Holsapple (1999) where flaws followed a power-law spanning many orders of magnitude. The top row in Fig. 2 shows images acquired through a high-speed camera during a dynamic Brazilian disk experiment ($30\ s^{-1}$) on a basalt sample, and the bottom row presents the damage profile in the corresponding MPM simulation. As the incident bar (on the left) compresses the sample, a tensile stress state is developed perpendicular to the loading direction. For a quasi-static test on a homogeneous, isotropic, and elastic material the maximum tensile stress would be at the geometric center of the specimen. In a dynamic test, wave interactions lead to a time-dependent shift in the location of maximum stress. Material heterogeneity also affects the location of the initial macro-scale crack nucleation. Consequently, at $t = 160\mu s$, the first subscale flaws are activated off-center but along the horizontal diameter. These cracks propagate orthogonal to the direction of maximum tensile stresses until fragmenting the disk. The damage profile at 220 μs is a typical failure pattern in Brazilian disk experiments (Zhou et al., 2014). The measured strengths are shown in Fig. 3 along with similar datasets from Housen (2009) and Nakamura et al. (2007) performed on different basalts. We estimate the strain rates of Nakamura et al. (2007) using the reported loading velocity and sample dimensions.

The numerical calculations were repeated for different simulated strain rates, and the computed dynamic tensile strengths are also shown in Fig. 3. These results illustrate the capability of the material model to reproduce tensile strengths within the same range as those seen in the experimental measurements, with a trend that replicates the strain-rate dependence of the strength, using only the flaw distribution as input.

4. Numerical simulation of asteroid impact

Now that we have demonstrated the material model's capability to capture strain-rate effects using a micromechanics definition of subscale crack growth, we seek to simulate hypervelocity impacts onto km-sized asteroids. We consider the case of a 1.21 km diameter impactor striking head-on a 25 km diameter target with an impact velocity of 5 km/s, with both the impactor and the target modeled as basalt monoliths. These initial conditions and impact configuration are, in essence, identical to that of Michel and Richardson (2013). The difference is in the material model used (Tonge–Ramesh), and the numerical scheme (MPM) and computational framework in which these are implemented (Uintah). Simulating the same impact allows us to assess the consequences of using a realistic material model that properly captures rate-dependent behavior. From a process perspective, we separate the problem of impact fragmentation and ejecta evolution into two subproblems based on their characteristic timescales. In the short-timescale fragmentation phase (up to a few tens of seconds), stress wave interactions dominate the problem, and so we use the MPM implementation of the Tonge–Ramesh material model. Beyond that time, gravitational forces become important and so we formulate a consistent hand-off scheme to transition the MPM results into the N-body gravity code, `pkdgrav`, which will capture the evolution of ejecta for the hours following impact.

4.1. Short-timescale fragmentation phase

We choose a background grid resolution that consists of $200 \times 200 \times 200$ m cells with 1 material point per cell. This resolution is equivalent to 3 particles per impactor radius and results in a little over 10^6 total particles in the system. Given the dimensions of the computational cell, we extend the initial flaw distribution to incorporate flaws as small as 1 cm and as large as 80 m with a flaw number density of 250 flaws/m^3. The 1 cm cut-off is chosen to maintain

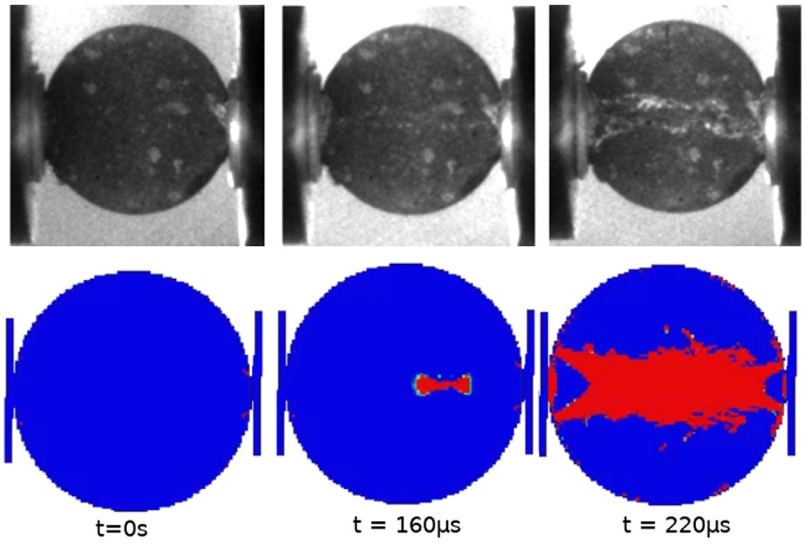

Fig. 2. The top row of images are acquired through a high-speed camera during a dynamic Brazilian disk experiment on a basalt sample (diameter is 10 mm). The bottom row shows a similar setup in MPM. The blue color refers to undamaged material, and the red is damaged material. The sample is dynamically compressed (by the incident plate on the left), and a state of local tension develops near the diameter's center. A crack initiates due to the tensile stresses (middle picture) and propagates towards the platens, leading to failure. (For interpretation of the references to colour in this figure legend, the reader is referred to the web version of this article.)

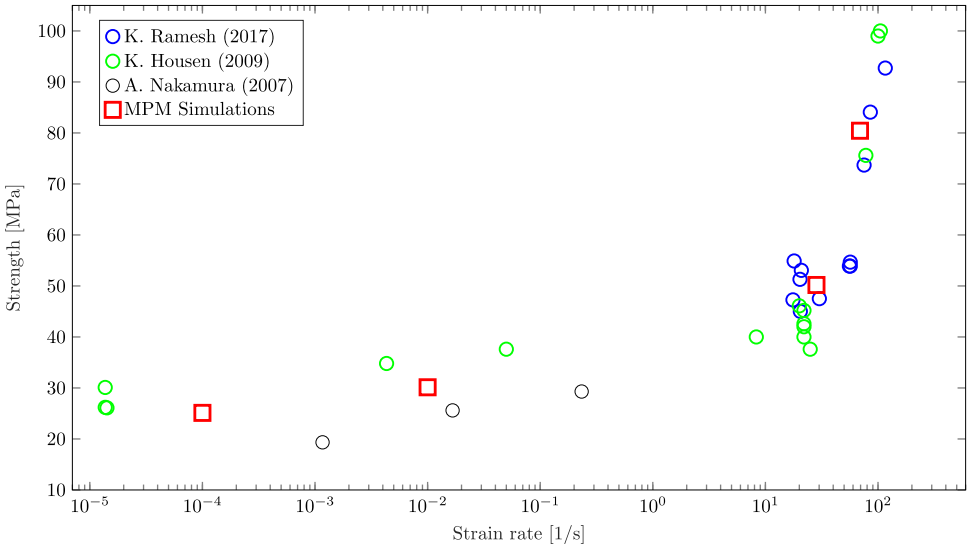

Fig. 3. Basalt tensile strength dependence on strain rate. Brazilian disk experiments (Ramesh et al., 2017). are plotted along with Housen (2009) and Nakamura et al. (2007). The Nakamura et al. (2007) strain rates are first-order estimates based on the platen loading speed and sample dimensions. Our model shows close agreement with the experimental data, especially at the higher strain rates.

a balance between resolving the sub-scale flaw size distribution and the available computational resources, whereas the 80 m upper limit is chosen to be consistent with the homogenization process at the material point level. The flaw number density for this larger crack size population is obtained using the same Pareto distribution as the simulations of the Brazil disk experiments (Table 1).

The direct computation of self-gravity is ignored during the failure phase occurring in the first few seconds following impact since the fragmentation timescale in this hypervelocity collision is orders of magnitudes smaller than the dynamical timescale for gravity (further, the lithostatic pressure is small compared to the shock wave amplitude). Instead, we approximate the gravity effect at these times by setting the overburden strength of the granular material to the gravitational overburden pressure at the center of the asteroid (Asphaug and Melosh, 1993; Tonge et al., 2016). This simplification overestimates the attractive force of gravity and underestimates the amount of porosity produced by the impact event. However for the timescales simulated in MPM, the dominant mechanisms are described in the material model, and the gravitational forces are much smaller than the inertial forces.

The fragmentation-phase calculation was carried out for a total simulated time of -37 s. One example of the typical outputs of the simulation are shown in Fig. 4 in terms of snapshots of the damage in the target at different times. Although these are full 3D Simulations, the figure shows 3/4 of the initially spherical target so that the evolution of internal damage can be observed. Note that sub-scale material heterogeneity breaks the symmetry of the problem. Each material particle is colored according to the degree of damage (Eq. (9)) in the particle. Note that granular flow begins in our material model when the damage parameter D reaches a value of 0.125, and the damage in a particle saturates at $D = 0.2$ (colored in red in Fig. 4).

Immediately after impact (2 s), a highly damaged region develops just and below the impact site while shock waves propagate deeper into the target. As these waves propagate further within the target ($4 - 6$ s), more sub-scale cracks are activated, and by ~ 6 s all material points in the target have sustained some level of damage high enough for the onset of granular flow. Notice that the damage profile is not axisymmetric due to the inherent variability in the flaw distributions that is incorporated in the model. The reflected waves from the free surface ($6 - 12$s) do not substantially change the overall damage profile since it is easier to grow preexisting cracks than it is to form new crack networks. By 18 s, the wave interactions from the impact have dissipated. Beginning around 12 s after impact, we observe ejecta coming from the impact site. These particles have speeds greater than 15 m/s, which exceeds the escape velocity on the surface of the body. Note that the "numerical fracture" limitation in the UGIMP implementation of the MPM equations that was discussed in the earlier section applies to these material points. The consequence here would be in overestimating the velocities of these particles as a trade-off to increased computational cost if we use *CPDI2*. In this simulation, only a small fraction of material points have been separated by a distance large enough for numerical fracture. These material points correspond to the high-velocity ejecta seen between 24–37 s in Fig. 4. We accept this limitation as these particles are unlikely to re-accumulate on the target and would not have a considerable impact on the damage and velocity profiles in the remainder of the target. A different treatment (such as using *CPDI2*) could be warranted when studying the formation of asteroid families or the low velocity ejecta in the context of asteroid mitigation simulations.

After 30 s, the entire target has been damaged to some degree, with the bulk of the damage on the side that was impacted. Note that the extent of the high damage (shown in red) is much larger within the body than is visible on the surface. A crater has been formed (not easily seen in the visualization), but note that our simulation was not designed with the resolution to investigate crater dynamics. Ejecta from the crater formation event includes high ejecta velocities, as previously discussed, and essentially all of the surface particles all around the target begin to move away from the surface at velocities that range from 5 to 20 m/s. However, there remains a large core of particles in the target that have been damaged but have very low velocities. That is, the entire target is not disrupted by the impact event. This is a key difference between our results and those of Michel and Richardson (2013). The damage profile and velocity fields have been fully established and the pressure at all material points is below the lithostatic pressure. This indicates that the dominant physics of the problem has transitioned from a wave interaction and stress-dominated problem to one dominated by gravity and rigid-body forces. We therefore choose this time as a cut-off for handing over the simulation data to `pkdgrav`.

4.2. *Hand-off from MPM to* `pkdgrav`

Once the pressures within the target become comparable to the gravitational overburden pressure, the system's evolution and the extent of reaccumulation are entirely determined by the velocity field of the individual fragments. The essential physics occuring in this longer timescale for reaccumulation can be properly captured by *N*-body gravity codes such as `pkdgrav` (Richardson et al., 2000; Stadel, 2001).

The results from our MPM runs need to be transitioned into a format suitable for *N*-body codes. In `pkdgrav`, materials are discretized into spheres. This spherical discretization requires having a set of well-

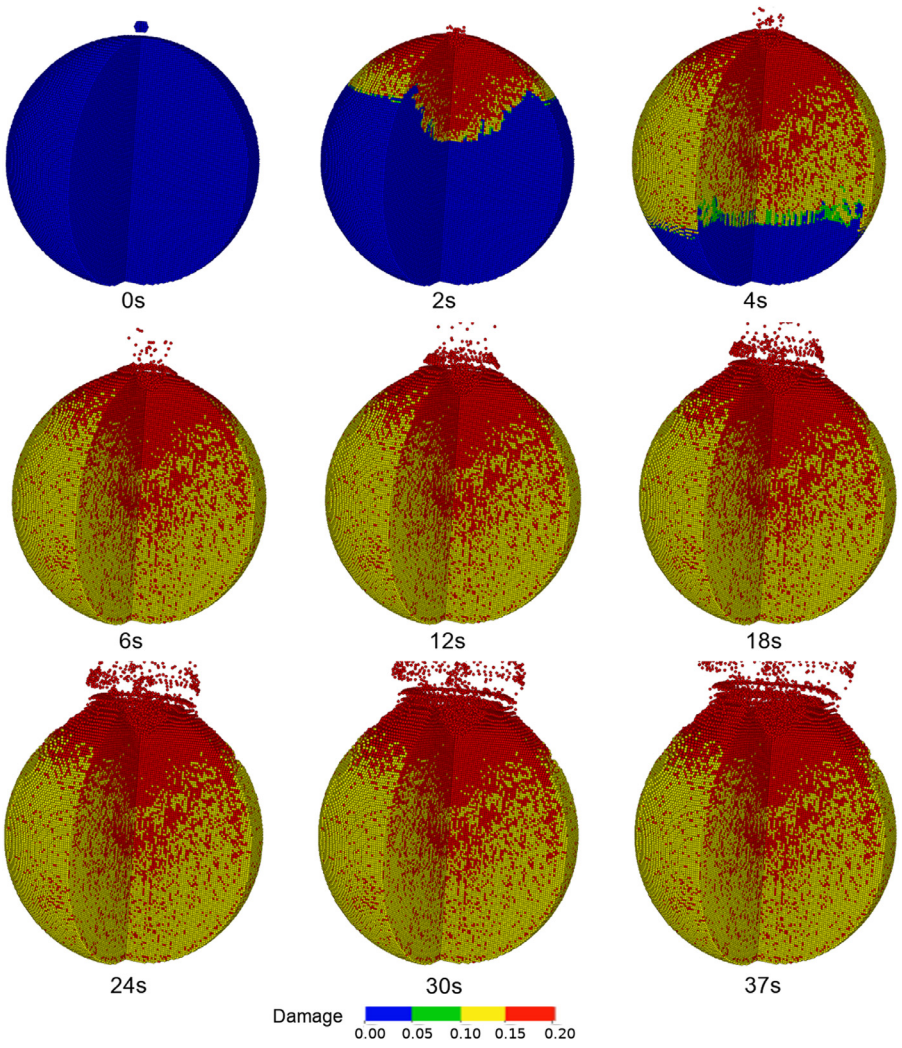

Fig. 4. Short timescale fragmentation phase simulations performed within an MPM framework (Uintah) of the 1.21 km diameter impactor striking the 25 km diameter target head-on at the upper hemisphere. While these are full 3D simulations, in these snapshots a quarter-slice of the spherical target is removed to visualize its interior. A highly damaged region (in red) develops under the impact site, along with some visible radial lineaments. The entire target develops some level of damage (colored yellow) and granular plasticity is activated at all material points. A damaged "core" of low-velocity particles forms near the target's center, which remains as the largest remnant in the long-timescale gravity simulations. We select $t = 30$ s as a cut-off time for the *N*-body gravity code hand-off. (For interpretation of the references to colour in this figure legend, the reader is referred to the web version of this article.)

formed elements that are non-overlapping or with extremely small overlaps as initial conditions in order to avoid unrealistic repulsive forces to reverse the overlap (Schwartz et al., 2016). Therefore, a consistent hand-off scheme is desirable that will ideally conserve the total momentum and energy of the system and result in a set of non-overlapping spheres at the initial step of the *N*-body simulation. We have developed such a consistent hand-off procedure, and this is described below and illustrated in the lower half of Fig. 1.

First, we determine the positions of the material points at the final timestep of the MPM simulation relative to the undeformed grid, consistent with the last step in the MPM algorithm (Fig. 1). We then interpolate the particle mass and momentum onto the background computational grid using the shape functions from MPM (Eqs. (1) and (3)). Nodal masses and velocities are calculated and interpolated back onto a single equivalent material point located at the center of each computational cell. Finally, the centered material point is transformed into a discrete sphere with a radius equal to half the grid cell length (last subplot in Fig. 1). The process is repeated for all MPM cells and the final data is written out into a format that can be processed in `pkdgrav`. This process conserves the total mass and momentum by construction. Small kinetic energy losses may occur in cells where a large number of material points are present, such as in highly compacted regions near the impact site. The order of this kinetic energy loss is equivalent to the energy dissipation in the MPM algorithm, which in our case is less than 1% of the total energy. In this hand-off, the projection of data from the material points to the grid preserves the total linear and angular momentum, but the total kinetic energy on the grid is less than the total kinetic energy in the material-points. The material-point-to-grid interpolation step dissipates kinetic energy, as do all GIMP implementations (which are either energy conserving or momentum conserving). This kinetic energy dissipation should always be quantified prior to running a `pkdgrav` simulation to ensure that the initial conditions in the gravity phase do not differ considerably from the last step of the MPM computation. The hand-off algorithm could be re-formulated to use a different sampling scheme in which the merging process results in two spherical particles instead of one, hence minimizing energy losses. Such advanced merging processes have been described in Vranic et al. (2015); Luu et al. (2016). In our case, the total energy lost in the hand-off process from MPM to `pkdgrav` was only 0.39%, and so we do not explore other algorithms for the hand-off. Note that a subsequent hand-off from `pkdgrav` back to MPM can be constructed in a similar manner and would allow the simulation of re-impact events following a reaccumulation stage.

In addition to the particle position, mass, and velocity, we also store the damage information by averaging the damage in each computational cell. In the long-timescale regime, we only use this damage value to label the "damaged" `pkdgrav` particles with different colors.

4.3. Long-timescale gravity phase

After the position, mass, velocity, and damage information from the final step of the MPM simulations are handed off to `pkdgrav`, we set up the second phase of the simulation that explicitly captures the gravitational interaction and evolution of the materials. We here use the so-

called “soft-sphere” discrete element method (SSDEM) (Schwartz et al., 2012), where the geometry is represented by a set of spherical particles that are allowed to have finite contact interaction times. SSDEM allows for the modeling of contact forces between particles in granular material, including rolling and twisting friction. Colliding spheres are allowed to slightly overlap and a linear spring-dashpot model is used to calculate the normal and tangential forces that oppose the deformation. This approach is different from that of Michel et al. (2001), in which the “hard-sphere” version of `pkdgrav` was used (Richardson et al., 2011). In a hard-sphere implementation, collisions are assumed to occur instantaneously at a single point of contact. The hard-sphere assumption allows for larger timesteps than SSDEM, at the expense of under-resolving the details of the mechanisms occuring during contact. We set up the material parameters to be typical gravel-like (Ballouz et al., 2015), which were extracted from avalanche experiments of streambed rocks (Yu et al., 2014). At this point, there is no material “strength” in the *N*-body gravity calculations. That is, gravitational attraction and frictional cohesion, including normal, tangential, rolling, and twisting (Zhang et al., 2017) frictions, are the only forces that tend to aggregate the particles. This “strengthless” approximation is likely to overestimate the evolution of the near-surface particle velocities, and the results of the `pkdgrav` calculation will be interpreted while being mindful to this limitation. The `pkdgrav` integration was carried out for a simulated time of 4.5 h using 120 computing cores running for 11 days. A second-order leapfrog integrator with a timestep of 5 ms is selected, which is limited by the particle velocities and the maximum allowed overlap (1% of the particle radius) in each timestep.

The results of the second-phase simulation are presented in Fig. 5, with the particles colored according to the degree of damage developed during the first phase of the simulations. In the first $\sim$ 15 min following impact, an ejection of near-surface material is observed. The majority of this ejecta blanket comes from the impact crater, although some particles as far as the end opposite to the impact site have also been mobilized. In the next hour, the low-speed ejecta begin to reaccumulate on the largest remnant, which remains held together throughout the entire gravity phase. In these runs, we observe a substantial ejecta fallback at the pole opposite to the impact site due to the particles that were launched at velocities just less than the escape velocity, which is consistent with predictions from scaling relations (Holsapple and Housen, 2012). By $\sim$ 2.5 h, almost 80% of the initial mass is recovered in the largest remnant. The surface of this largest remnant is covered with the `pkdgrav` particles labeled in red, which were the most heavily fragmented particles where granular flow was most active in the MPM simulations. By $\sim$ 3 h after impact, most of the reaccumulation events have occurred and the largest remnant is observed to be displacing vertically downwards due to the transfer of linear momentum. Some far-field particles may eventually cluster together to form smaller secondary asteroids, but our calculations did not run for long enough to capture such events. The mass ratio of the largest remnant to the parent body after 4 h was $M_{LR}/M_{PB} = 0.85$, a much higher value than the 0.5 that is taken as a reference for disruption limit calculations. Note also the distinctive shape of the largest remnant in this non-rotating case (we will address rotating targets in a subsequent manuscript). It is also apparent that the spatial distribution of damaged particles evolves as a result of the reaccumulation phase. The evolution of the spatial distribution of damage in the target is shown in Fig. 6 for three specific times: 3 s after impact, 30 s after impact, and 7230 s after impact (2 h after hand-off).

The predicted damage in the target is presented as a function of distance along the diameter, looking along the direction of impact. Note that the maximum value of damage allowed by the model is 0.2. Three seconds after impact, the region immediately beneath the impactor is fully damaged, but a significant fraction of the target is completely undamaged. At 30 s, all particles along the diameter have developed some level of damage, with a highly damaged region reaching a depth of almost 10 km. At 2 h after the hand-off to `pkdgrav`, the high-velocity particles from under the impact site have been ejected and new surfaces have been exposed. This excavation is manifested in a shift to the left of the curve (notice the damage “dip” has moved from a depth of 10 km to around 5 km). In addition, the reaccumulation of mostly

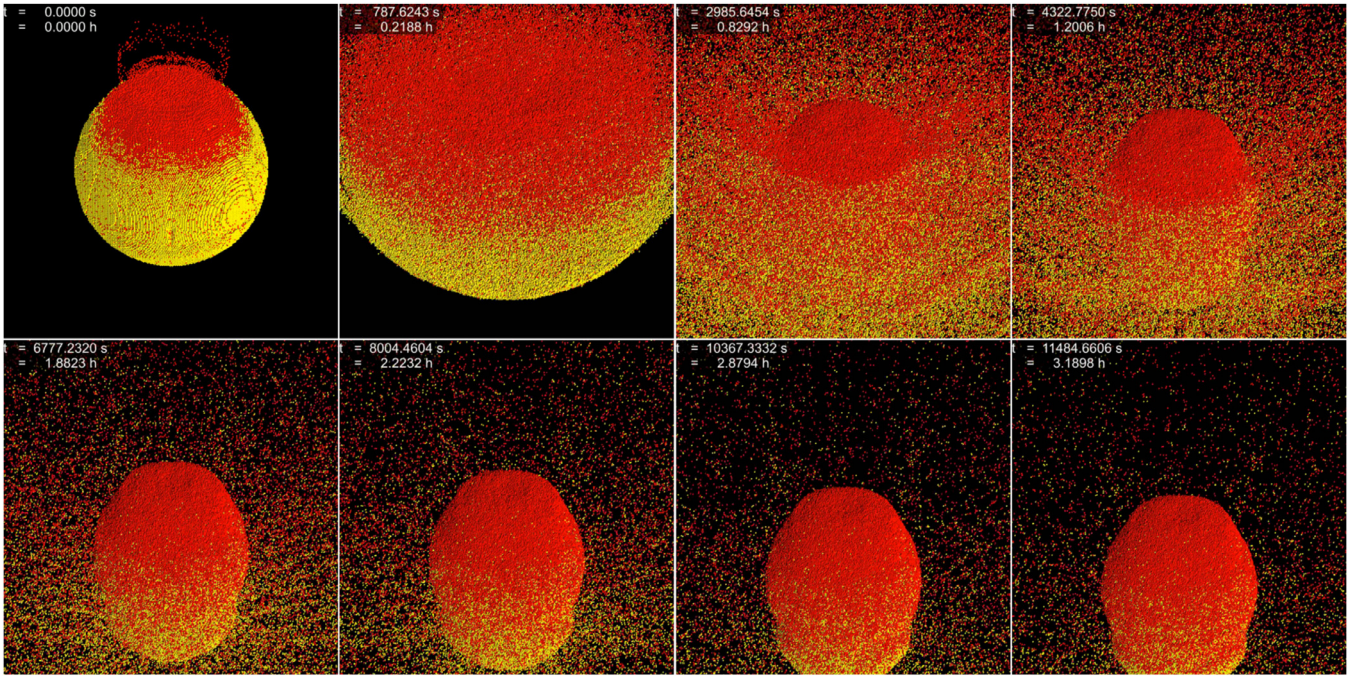

Fig. 5. Snapshots of the `pkdgrav` computations at different simulated times. The colors represent different damage levels, consistent with Fig. 4. *Note* that here $t = 0s$ refers to the beginning of the long-timescale gravity phase. In view of this hybrid MPM/`pkdgrav` approach, this time is in fact at 30 s post-impact, which is the hand-off time from MPM. A violent ejection of surface material is observed during the first hour, followed by a reaccumulation phase. Throughout the entire gravity-timescale simulations, the heavily fractured “core” remains bound by gravity. The target is seen to be moving vertically downwards due to the momentum imparted to it.

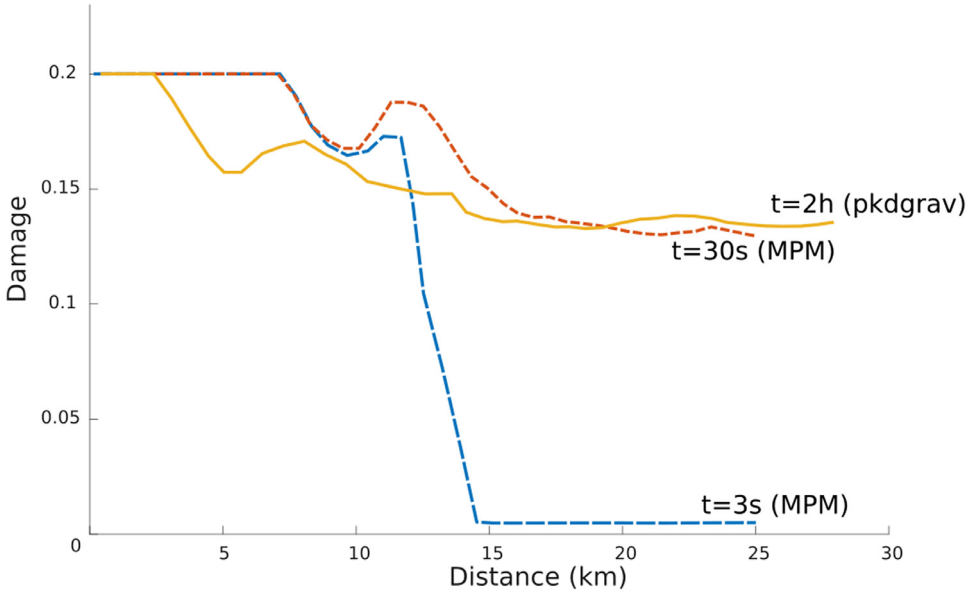

Fig. 6. Predicted damage in the target as a function of distance along the diameter, in the direction of the impact. The dashed lines represent data extracted from the short-timescale (MPM) phases, and the solid line is from the long-timescale (`pkdgrav`) reaccumulation stage.

damaged particles at the target end opposite to the impact location is manifested as an extension of the original 25 km diameter to around 28 km. This new damage profile remains largely unchanged thereafter. Such predicted damage profiles may be useful in mission planning.

5. Discussion

Using this new hybrid MPM/`pkdgrav` approach, we simulated the impact of a 1.21 km diameter basalt asteroid onto a 25 km diameter basalt target. We track the material response from material deformation and fragmentation through to gravitational ejection and reaccumulation. In contrast to SPH calculations with similar initial conditions, the 5 km/s impact does not lead to the complete shattering of the target (the SPH calculations of Michel and Richardson (2013) led to fragmentation down to the smallest numerical resolution). Instead, our impact outcome shows a heavily damaged but coherent "core" under the impact site. The key difference between this work and Michel and Richardson (2013) in the fragmentation phase is in the implemented (and validated) constitutive model. Here, the micromechanics definition of damage leads to inherent strain-rate dependence of the strength and deterioration of elastic moduli. Further, a "damaged" material is not generally "strengthless". Furthermore, an initially non-porous target would develop internal porosity as the material is fragmented. Both the granular flow through shearing of damaged material, and the crushing of pores due to pressure, constitute mechanisms for energy dissipation. In effect, the damage profile in Fig. 4 does not change substantially from 6 s to 30 s since further cracking of grains is less energetically favorable than the flow of fragments. Our model suggests that asteroids, even initially monolithic and non-porous ones, are "stronger" than is traditionally assumed. Impacts would have to occur at larger specific energies to reach complete disruption.

In the long-timescale gravity calculation, the fragmented "core" acted akin to a gravity well over which ejecta reaccumulated. Substantial ejecta fallback occurred at the pole opposite to the impact site, whereas an excavated surface emerged from beneath the impact location. The internal damage distribution in the asteroid after the ejecta reaccumulation phase shows the signature of both the impact and the fallback of damaged ejecta. The results indicate that such asteroids could have an interior that is a heavily fragmented shard of an initially intact parent body following a first impact. Additionally, they could have substantial porosity while not necessarily being a rubble pile of gravitationally bound reaccumulated fragments. Note that subsequent impacts may further break down, and possibly disrupt, the largest remnant.

The impact simulation examined in this work and in Michel and Richardson (2013) correspond to a specific impact energy of 1.13×10^8 erg/g. In the Michel and Richardson (2013) simulation, the largest remnant after gravitational accumulation had a mass ratio relative to the parent body of $M_{LR}/M_{PB} = 0.5$, which means that this impact is at the specific energy for disruption (Q_D^*). A similar disruption threshold measure was previously obtained by Benz and Asphaug (1999) for impacts onto basalt with the same initial conditions. In contrast, the mass ratio of the largest remnant in our simulations was much larger, with $M_{LR}/M_{PB} = 0.85$, meaning that this specific impact energy is smaller than the disruption threshold that would be predicted by our model. This indicates that intact monolithic parent asteroids may have a higher disruption threshold, Q_d^*, than previously expected and require higher impact energies to be completely shattered. The limits of this observation for smaller targets remains to be explored, and we plan to use our model in a later work to explore the disruption threshold over a range of target sizes.

In our simulation, the damage profile does not evolve much further following the activation of the granular flow, which is more energetically favorable than continued fragmentation. In addition, porosity is introduced as the initial shock wave travels through the body, and so the reflected wave amplitude is dampened due to this porosity. In that sense, both the pore compaction and the granular flow process are dissipative processes, and a parametric study will be required to isolate the roles of these different factors. The difference in the damage profile of this study and that of Michel and Richardson (2013) could be due to both the interaction and rate-dependent growth of subscale flaws, and the energy dissipative mechanisms associated with the activation of granular flow and dilatation. These observations are similar to those of Jutzi et al. (2010); Jutzi (2015) where a significant increase in the catastrophic disruption threshold was noted due to energy dissipation through friction and pore crushing in granular material.

In contrast to Michel and Richardson (2013) and Jutzi et al. (2010), this work uses the soft-sphere implementation of `pkdgrav`, which has a better handle on individual fragment geometries and impact forces as opposed to the hard-sphere method where fragment collisions are treated as bounces or mergers resulting in a new spherical particle with a combined mass and equivalent diameter. The gravity response is

therefore expected to be different, especially in terms of the formation of gravitationally-bound aggregates. For the impact conditions considered in this work, we do not observe the formation of any asteroid families. However, the far-field ejecta could accumulate to form small secondary aggregates at much later times beyond those reached in our simulations.

In Fig. 5, the target can be seen moving vertically downwards as a result of the momentum imparted by the impactor. The momentum enhancement factor is calculated to be $\beta = 1.69$, which is much smaller than previous estimates of impacts onto competent rocks (Holsapple and Housen, 2012; Housen and Holsapple, 2015). The low momentum enhancement in this case is primarily a result of the large amount of ejecta reaccumulation occurring in the gravity phase.

The consistent hand-off employed in our hybrid approach allows us to identify individual `pkdgrav` particles and map them back to their equivalent MPM particle. For instance, in this work the value of the damage parameter (Eq. (9)) from MPM is stored as an additional label in `pkdgrav` that we use to color-code the SSDEM spheres. Additionally, internal MPM state variables from the short-timescale fragmentation phase can be preserved throughout the `pkdgrav` simulations. A hand-off from `pkdgrav` to MPM can then be similarly performed for simulating subsequent impacts. Such a capability would be beneficial for detailed collisional history studies.

One caveat in the current work is that the target in the long-timescale gravity stage is modeled as an aggregate of spheres with no tensile strength. This is an oversimplication of the material state at the end of the MPM simulation where tensile strength is still present. In previous work (Michel et al., 2001, 2002, 2003; Michel and Richardson, 2013), such an assumption was justified given that all particles, down to the numerical resolution, were fragmented at the end of the SPH calculations. However, we note here that not all of the MPM particles were fully damaged by the time for hand-off. This simplification in the `pkdgrav` stage would likely lead to an overestimated velocity for the surface particles, partially causing the violent ejection seen during the first timesteps of Fig. 5. Schwartz et al. (2013) presented an implementation of strength in `pkdgrav` by bonding neighboring particles' centers of mass with "springs" that result in a restoring force opposing the distention of the bonds. This implementation comes with an additional computational expense since the timesteps would be limited by the oscillation half-period of the spring (Schwartz et al., 2012). One could use such a spring-based bonding approximation, and use the damage parameter from the MPM simulation as an indicator for the deterioration in the initial spring stiffnesses in `pkdgrav`. In future runs, we will be looking at the effects of strength in the long-timescale gravity regime (Zhang et al., 2018).

Finally, we note that we do not experience any difficulties in MPM with capturing the low-velocity ejecta. The standard SPH formulation is often reported to induce small-scale sub-sonic velocity noise as a consequence of the gradient estimate error in SPH (Bauer and Springel, 2012). This numerical noise was also mentioned as an encountered difficulty in the work of Schwartz et al. (2016) exploring Didymoon-scale impacts in the context of the DART mission. Given the scale of the target, its low escape speed, and the high impact velocity, the computation of the ejecta velocities become close to the numerical noise of the SPH simulations. Schwartz et al. (2016) also notes that the results were affected by the wave reflections at the boundary of their discretized domain. In MPM, however, the use of a background grid for gradient calculations eliminates these gradient estimate errors. The coupled approach presented here may therefore be used to model the fate of low-speed reaccumulation in situations such as on Didymoon in the context of the DART mission.

6. Summary

We have presented a new coupled MPM/`pkdgrav` hybrid approach to simulate the collisional evolution of rocky asteroids from the early fragmentation stages to the later times of gravitational reaccumulation. A modified version of the Tonge–Ramesh material model that includes the Tillotson equation of state was implemented in an MPM framework to capture the material response for the first tens of seconds following impact. A consistent hand-off scheme was formulated to transition to the *N*-body gravity code `pkdgrav` for integrating the long-timescale gravity effects.

The multi-physics material model is centered around the growth mechanism of an initial distribution of subscale flaws. Rate effects in the model are a natural outcome of the limited crack growth speed, which is explicitly computed based on the local stress state. In addition, porosity growth, pore compaction, and granular flow of highly damaged materials are captured at the material-point level. We validated the model's predictive capability by comparing the dynamic tensile strength with high-strain-rate Brazilian disk experiments performed on basalt samples.

As an application of the hybrid technique, we considered an asteroid impact with initial conditions similar to Michel and Richardson (2013). In contrast to previous results, the impact event did not lead to the complete disruption of the target. The collision imparted substantial damage onto the target, with most of the damage localized under the impact site, resulting in a heavily fractured but not fully damaged "core". The material points were then converted into soft spheres and handed over to `pkdgrav` in a self-consistent manner to calculate the gravitational interaction of the ejected material. We observed substantial ejecta fallback onto the largest remnant of the parent body, with a recovered mass of the largest remnant being 0.85 that of the parent body, indicating that the disruption thresholds for such targets may be higher than previously thought.

The framework presented in this study can be applied to a variety of asteroid impact and deflection scenarios. In the future, we plan to incorporate a tensile strength model in the *N*-body simulations and use this newly developed framework to explore the disruption thresholds for a range of target sizes. We are also looking at applying the model for studying impacts onto initially rotating targets and their effects on the collisional evolution of asteroids and asteroid families.

Acknowledgments

The authors would like to thank the Solar System Exploration Research Virtual Institute (SSERVI) for providing financial support for the current study through NASA Cooperative Agreement NNA14AB02A. The authors thank Dr. A. Stickle (APL) for providing the raw data for the brazilian disk experiments presented in this work. We also acknowledge Dr. O. Barnouin (APL) for constructive discussions and feedback during this investigation. The authors gratefully acknowledge the Uintah development team for developing, maintaining, and providing the computational platform to the public as open-source software. Part of this material is based on work supported by the U.S. National Aeronautics and Space Administration under grant no. NNX15AH90G.

Supplementary material

Supplementary material associated with this article can be found, in the online version, at doi:10.1016/j.icarus.2018.12.032.

References

Asphaug, E., 2009. Growth and evolution of asteroids. Annu. Rev. Earth Planet Sci. 37, 413–448. https://doi.org/10.1146/annurev.earth.36.031207.124214.

Asphaug, E., Melosh, H.J., 1993. The stickney impact of phobos: a dynamical model. Icarus 101 (1), 144–164. https://doi.org/10.1006/icar.1993.1012.

Asphaug, E., Ryan, E.V., Zuber, M.T., 2002. Asteroid interiors. Asteroids III. 1. University. of Arizona, Tucson, pp. 463–484.

Ballouz, R.-L., Richardson, D.C., Michel, P., Schwartz, S.R., Yu, Y., 2015. Numerical simulations of collisional disruption of rotating gravitational aggregates: dependence

on material properties. Planet. Space Sci. 107, 29–35. https://doi.org/10.1016/j.pss.2014.06.003.
Balme, M.R., Rocchi, V., Jones, C., Sammonds, P.R., Meredith, P.G., Boon, S., 2004. Fracture toughness measurements on igneous rocks using a high-pressure, high-temperature rock fracture mechanics cell. J. Volcanol. Geotherm. Res. 132 (2–3), 159–172. https://doi.org/10.1016/S0377-0273(03)00343-3.
Bardenhagen, S.G., Brackbill, J.U., Sulsky, D., 2000. Numerical study of stress distribution in sheared granular material in two dimensions. Phys. Rev. E Stat. Phys. Plasmas Fluids Relat. Interdiscip. Top. 62 (3 B), 3882–3890. https://doi.org/10.1103/PhysRevE.62.3882.
Bardenhagen, S.G., Brackbill, J.U., Sulsky, D., 2000. The material-point method for granular materials. Comput. Methods Appl. Mech. Eng. 187 (3–4), 529–541. https://doi.org/10.1016/S0045-7825(99)00338-2.
Bardenhagen, S.G., Guilkey, J.E., Roessig, K.M., Brackbill, J.U., Witzel, W.M., Foster, J.C., 2001. An improved contact algorithm for the material point method and application to stress propagation in granular material. CMES Comput. Model. Eng. Sci. 2 (4), 509–522.
Bardenhagen, S.G., Kober, E.M., 2004. The generalized interpolation material point method 2. Comput. Model. Eng. Sci. 5 (6), 477–495. https://doi.org/10.3970/cmes.2004.005.477.
Barucci, M.A., Dotto, E., Levasseur-Regourd, A.C., 2011. Space missions to small bodies: asteroids and cometary nuclei. Astron. Astrophys. Rev. 19 (1), 48. https://doi.org/10.1007/s00159-011-0048-2.
Bauer, A., Springel, V., 2012. Subsonic turbulence in smoothed particle hydrodynamics and moving-mesh simulations. Mon. Not. R Astron. Soc. 423 (3), 2558–2578. https://doi.org/10.1111/j.1365-2966.2012.21058.x.
Benz, W., Asphaug, E., 1994. Impact simulations with fracture. I. method and tests. Icarus 107 (1), 98–116. https://doi.org/10.1006/icar.1994.1009.
Benz, W., Asphaug, E., 1995. Simulations of brittle solids using smooth particle hydrodynamics. Comput. Phys. Commun. 87 (1–2), 253–265. https://doi.org/10.1016/0010-4655(94)00176-3.
Benz, W., Asphaug, E., 1999. Catastrophic disruptions revisited. Icarus 142 (1), 5–20. https://doi.org/10.1006/icar.1999.6204. arXiv:9907117.
Boyce, B.L., Kramer, S.L.B., Fang, H.E., Cordova, T.E., Neilsen, M.K., Dion, K., Kaczmarowski, A.K., Karasz, E., Xue, L., Gross, A.J., Others, 2014. The sandia fracture challenge: blind round robin predictions of ductile tearing. Int. J. Fract. 186 (1–2), 5–68. https://doi.org/10.1007/s10704-013-9904-6.
Brackbill, J.U., Kothe, D.B., Ruppel, H.M., 1988. FLIP: a low-dissipation, particle-in-cell method for fluid flow. Comput. Phys. Commun. 48 (1), 25–38. https://doi.org/10.1016/0010-4655(88)90020-3.
Brackbill, J.U., Ruppel, H.M., 1986. FLIP: A method for adaptively zoned, particle-in-cell calculations of fluid flows in two dimensions. J. Comput. Phys. 65 (2), 314–343. https://doi.org/10.1016/0021-9991(86)90211-1.
Cheng, A.F., Atchison, J., Kantsiper, B., Rivkin, A.S., Stickle, A., Reed, C., Galvez, A., Carnelli, I., Michel, P., Ulamec, S., 2015. Asteroid impact and deflection assessment mission. Acta Astron. 115, 262–269. https://doi.org/10.1016/j.actaastro.2015.05.021.
Durda, D.D., Bottke, W.F., Enke, B.L., Merline, W.J., Asphaug, E., Richardson, D.C., Leinhardt, Z.M., 2004. The formation of asteroid satellites in large impacts: results from numerical simulations. Icarus 170 (1), 243–257.
Durda, D.D., Bottke, W.F., Nesvorný, D., Enke, B.L., Merline, W.J., Asphaug, E., Richardson, D.C., 2007. Size-frequency distributions of fragments from SPH/N-body simulations of asteroid impacts: comparison with observed asteroid families. Icarus 186 (2), 498–516. https://doi.org/10.1016/j.icarus.2006.09.013.
Ganpule, S., Daphalapurkar, N.P., Ramesh, K.T., Knutsen, A.K., Pham, D.L., Bayly, P.V., Prince, J.L., 2017. A three-Dimensional computational human head model that captures live human brain dynamics. J. Neurotrauma 34 (13), 2154–2166. https://doi.org/10.1089/neu.2016.4744.
Germain, J.D.d.S., McCorquodale, J., Parker, S.G., Johnson, C.R., 2000. Uintah: a massively parallel problem solving environment. Proceedings of the Ninth International Symposium on High-Performance Distributed Computing. IEEE, pp. 33–41.
Grady, D.E., Kipp, M.E., 1980. Continuum modelling of explosive fracture in oil shale. Int. J. Rock Mech. Min. Sci. Geomechan. Abstr. 17, 147–157. https://doi.org/10.1016/0148-9062(80)90765-2.
Grady, D.E., Lipkin, J., 1980. Criteria for impulsive rock fracture. Geophys. Res. Lett. 7 (4), 255–258. https://doi.org/10.1029/gl007i004p00255.
Guilkey, J., Harman, T., Luitjens, J., Schmidt, J., Thornock, J., de St Germain, J.D., Shankar, S., Peterson, J., Brownlee, C., Reid, C., Others, 2009. Uintah User Guide. Technical Report. SCI Institute Technical Report.
Hérique, A., Agnus, B., Asphaug, E., Barucci, A., Beck, P., Bellerose, J., Biele, J., Bonal, L., Bousquet, P., Bruzzone, L., Others, 2017. Direct observations of asteroid interior and regolith structure: science measurement requirements. Adv. Space Res. https://doi.org/10.1016/j.asr.2017.10.020.
Holsapple, K.A., Housen, K.R., 2012. Momentum transfer in asteroid impacts. I. theory and scaling. Icarus 221 (2), 875–887. https://doi.org/10.1016/j.icarus.2012.09.022.
Housen, K., 2009. Dynamic strength measurements on granite and basalt. Proceedings of the Lunar and Planetary Science Conference. 40. pp. 1701.
Housen, K.R., Holsapple, K.A., 1999. Scale effects in strength-Dominated collisions of rocky asteroids. Icarus 142 (1), 21–33. https://doi.org/10.1006/icar.1999.6206.
Housen, K.R., Holsapple, K.A., 2015. Experimental measurements of momentum transfer in hypvelocity collisions. Proceedings of the Lunar and Planetary Science Conference. 46. pp. 2–3.
Huq, F., Brannon, R., Graham-Brady, L., 2016. An efficient binning scheme with application to statistical crack mechanics. Int. J. Numer. Methods Eng. 105 (1), 33–62.
Ionescu, I., Guilkey, J.E., Berzins, M., Kirby, R.M., Weiss, J.A., 2006. Simulation of soft tissue failure using the material point method. J. Biomech. Eng. 128 (6), 917–924. https://doi.org/10.1115/1.2372490.
Jutzi, M., 2015. SPH Calculations of asteroid disruptions: the role of pressure dependent failure models. Planet Space Sci. 107, 3–9. https://doi.org/10.1016/j.pss.2014.09.012.
Jutzi, M., Benz, W., Michel, P., 2008. Numerical simulations of impacts involving porous bodies: i. implementing sub-resolution porosity in a 3D SPH hydrocode. Icarus 198 (1), 242–255.
Jutzi, M., Michel, P., Benz, W., Richardson, D.C., 2010. Fragment properties at the catastrophic disruption threshold: the effect of the parent body's internal structure. Icarus 207 (1), 54–65. https://doi.org/10.1016/j.icarus.2009.11.016. arXiv:0911.3937.
Jutzi, M., Michel, P., Hiraoka, K., Nakamura, A.M., Benz, W., 2009. Numerical simulations of impacts involving porous bodies: II. comparison with laboratory experiments. Icarus 201 (2), 802–813.
Kimberley, J., Ramesh, K.T., 2011. The dynamic strength of an ordinary chondrite. Meteor. Planet. Sci. 46 (11), 1653–1669.
Kimberley, J., Ramesh, K.T., Daphalapurkar, N.P., 2013. A scaling law for the dynamic strength of brittle solids. Acta Mater 61 (9), 3509–3521. https://doi.org/10.1016/j.actamat.2013.02.045.
Kupchella, R., Stowe, D., Weiss, M., Pan, H., Cogar, J., 2015. SPH Modeling improvements for hypervelocity impacts. Procedia. Eng. 103, 326–333. https://doi.org/10.1016/j.proeng.2015.04.054.
Lawrence, R.J., 1990. Enhanced momentum transfer from hypervelocity particle impacts. Int. J. Impact. Eng. 10 (1), 337–349. https://doi.org/10.1016/0734-743x(90)90070-c.
Li, D.Y., Wong, L.N.Y., 2013. The brazilian disc test for rock mechanics applications: review and new insights. Rock Mech. Rock Eng. 46 (2), 269–287. https://doi.org/10.1007/s00603-012-0257-7.
Lindholm, U.S., Yeakley, L.M., Nagy, A., 1974. The dynamic strength and fracture properties of dresser basalt. Int. J. Rock Mech. Min. Sci. Geomechan. Abstr. 11, 181–191. https://doi.org/10.1016/0148-9062(74)93145-3.
Luu, P.T., Tückmantel, T., Pukhov, A., 2016. Voronoi particle merging algorithm for PIC codes. Comput. Phys. Commun. 202, 165–174. https://doi.org/10.1016/j.cpc.2016.01.009.
Martin, B.E., Kabir, M.E., Chen, W., 2013. Undrained high-pressure and high strain-rate response of dry sand under triaxial loading. Int. J. Impact. Eng. 54, 51–63. https://doi.org/10.1016/j.ijimpeng.2012.10.008.
Melosh, H.J., Ryan, E.V., Asphaug, E., 1992. Dynamic fragmentation in impacts: hydrocode simulation of laboratory impacts. J. Geophys. Res. Plan. 97 (E9), 14735–14759. https://doi.org/10.1029/92je01632.
Michel, P., Benz, W., Richardson, D.C., 2003. Disruption of fragmented parent bodies as the origin of asteroid families. Nature 421 (6923), 608–611. https://doi.org/10.1038/nature01364.
Michel, P., Benz, W., Tanga, P., Richardson, D.C., 2001. Collisions and gravitational reaccumulation: forming asteroid families and satellites. Science 294 (5547), 1696–1700. https://doi.org/10.1126/science.1065189.
Michel, P., Richardson, D.C., 2013. Collision and gravitational reaccumulation: possible formation mechanism of the asteroid Itokawa. Astron. Astrophys. 554, L1. https://doi.org/10.1051/0004-6361/201321657.
Michel, P., Tanga, P., Benz, W., Richardson, D.C., 2002. Formation of asteroid families by catastrophic disruption: simulations with fragmentation and gravitational reaccumulation. Icarus 160 (1), 10–23. https://doi.org/10.1006/icar.2002.6948.
Nakamura, A., Fujiwara, A., 1991. Velocity distribution of fragments formed in a simulated collisional disruption. Icarus 92 (1), 132–146. https://doi.org/10.1016/0019-1035(91)90040-z.
Nakamura, A.M., Michel, P., Setoh, M., 2007. Weibull parameters of Yakuno basalt targets used in documented high-velocity impact experiments. J. Geophys. Res. E Planet 112 (2). https://doi.org/10.1029/2006JE002757.
O'Keefe, J., Ahrens, T., 1982. The interaction of the cretaceous/tertiary extinction bolide with the atmosphere, ocean, and solid earth. Geol. Soc. Am. Spec. Pap. 190 (.), 103–120. https://doi.org/10.1130/SPE190-p103.
Paliwal, B., Ramesh, K.T., 2008. An interacting micro-crack damage model for failure of brittle materials under compression. J. Mech. Phys. Solids 56 (3), 896–923. https://doi.org/10.1016/j.jmps.2007.06.012.
Prockter, L., Thomas, P., Robinson, M., Joseph, J., Milne, A., Bussey, B., Veverka, J., Cheng, A., 2002. Surface expressions of structural features on eros. Icarus 155 (1), 75–93. https://doi.org/10.1006/icar.2001.6770.
Ramesh, K.T., 2009. High strain rate and impact experiments. Springer Handbook of Experimental Solid Mechanics. Springer, 101 Philip Drive, Norwell MA 02061, USA, pp. 929–959.
Ramesh, K.T., Stickle, A.M., Kimberley, J., 2017. Rocks, shocks and asteroids, and some interesting research directions in mechanics. Exp. Mech. 57 (8), 1149–1159. https://doi.org/10.1007/s11340-017-0324-9.
Richardson, D.C., Michel, P., Walsh, K.J., Flynn, K.W., 2009. Numerical simulations of asteroids modelled as gravitational aggregates with cohesion. Planet Space Sci. 57 (2), 183–192. https://doi.org/10.1016/j.pss.2008.04.015.
Richardson, D.C., Quinn, T., Stadel, J., Lake, G., 2000. Direct large-scale N-body simulations of planetesimal dynamics. Icarus 143 (1), 45–59. https://doi.org/10.1006/icar.1999.6243.
Richardson, D.C., Walsh, K.J., Murdoch, N., Michel, P., 2011. Numerical simulations of granular dynamics: i. hard-sphere discrete element method and tests. Icarus 212 (1), 427–437. https://doi.org/10.1016/j.icarus.2010.11.030. arXiv:1306.2528.
Sadeghirad, A., Brannon, R.M., Burghardt, J., 2011. A convected particle domain interpolation technique to extend applicability of the material point method for problems involving massive deformations. Int. J. Numer. Methods Eng. 86 (12), 1435–1456. https://doi.org/10.1002/nme.3110.

Schwartz, S.R., Michel, P., Richardson, D.C., 2013. Numerically simulating impact disruptions of cohesive glass bead agglomerates using the soft-sphere discrete element method. Icarus 226 (1), 67–76. https://doi.org/10.1016/j.icarus.2013.05.007.

Schwartz, S.R., Richardson, D.C., Michel, P., 2012. An implementation of the soft-sphere discrete element method in a high-performance parallel gravity tree-code. Granul. Matter 14 (3), 363. https://doi.org/10.1007/s10035-012-0346-z.

Schwartz, S.R., Yu, Y., Michel, P., Jutzi, M., 2016. Small-body deflection techniques using spacecraft: techniques in simulating the fate of ejecta. Adv. Space Res. 57 (8), 1832–1846. https://doi.org/10.1016/j.asr.2015.12.042.

Stadel, J.G., 2001. Cosmological N-body simulations and their analysis. University of Washington Washington, DC.

Sulsky, D., Chen, Z., Schreyer, H.L., 1994. A particle method for history-dependent materials. Comput. Methods Appl. Mech. Eng. 118 (1–2), 179–196. https://doi.org/10.1016/0045-7825(94)90112-0.

Sulsky, D., Zhou, S.J., Schreyer, H.L., 1995. Application of a particle-in-cell method to solid mechanics. Comput. Phys. Commun. 87 (1–2), 236–252. https://doi.org/10.1016/0010-4655(94)00170-7.

Swegle, J.W., Hicks, D.L., Attaway, S.W., 1995. Smoothed particle hydrodynamics stability analysis. J. Comput. Phys. 116 (1), 123–134. https://doi.org/10.1006/jcph.1995.1010.

Tillotson, J.H., 1962. Metallic equations of state for hypervelocity impact. Technical Report. General Atomic, Division of General Dynamics, San Diego, CA.

Tonge, A.L., Kimberley, J., Ramesh, K., 2013. A consistent scaling framework for simulating high rate brittle failure problems. Proced. Eng. 58, 692–701.

Tonge, A.L., Ramesh, K., 2016. Multi-scale defect interactions in high-rate brittle material failure. part i: model formulation and application to ALON. J. Mech. Phys. Solids 86 (Supplement C), 117–149. https://doi.org/10.1016/j.jmps.2015.10.007.

Tonge, A.L., Ramesh, K.T., Barnouin, O., 2016. A model for impact-induced lineament formation and porosity growth on eros. Icarus 266, 76–87. https://doi.org/10.1016/j.icarus.2015.11.018.

Vardar, O., Finnie, I., 1977. The prediction of fracture in brittle solids subjected to very short duration tensile stresses. Int. J. Fract. 13 (2), 115–131. https://doi.org/10.1007/BF00042555.

Vranic, M., Grismayer, T., Martins, J., Fonseca, R., Silva, L., 2015. Particle merging algorithm for PIC codes. Comput. Phys. Commun. 191, 65–73. https://doi.org/10.1016/j.cpc.2015.01.020.

Walker, J.D., Chocron, S., 2011. Momentum enhancement in hypervelocity impact. Int. J. Impact. Eng. 38 (6), A1–A7. https://doi.org/10.1016/j.ijimpeng.2010.10.026.

Weibull, W., 1939. A Statistical Theory of the Strength of Materials. Handlingar / Ingeniörs Vetenskaps Akademien 151 Generalstabens litografiska anstalts förlag ISSN: 0368-069X.

Weibull, W., 1951. A statistical distribution function of wide applicability. J. Appl. Mech. 18 (730), 293–297. doi:citeulike-article-id:8491543.

Wilkison, S.L., Robinson, M.S., Thomas, P.C., Veverka, J., McCoy, T.J., Murchie, S.L., Prockter, L.M., Yeomans, D.K., 2002. An estimate of Eros's porosity and implications for internal structure. Icarus 155 (1), 94–103. https://doi.org/10.1006/icar.2001.6751.

Yu, Y., Richardson, D.C., Michel, P., Schwartz, S.R., Ballouz, R.-L., 2014. Numerical predictions of surface effects during the 2029 close approach of asteroid 99942 apophis. Icarus 242 (Supplement C), 82–96. https://doi.org/10.1016/j.icarus.2014.07.027.

Zhang, Y., Richardson, D.C., Barnouin, O.S., Maurel, C., Michel, P., Schwartz, S.R., Ballouz, R.-L., Benner, L.A.M., Naidu, S.P., Li, J., 2017. Creep stability of the proposed AIDA mission target 65803 didymos: I. discrete cohesionless granular physics model. Icarus 294, 98–123. https://doi.org/10.1016/j.icarus.2017.04.027.

Zhang, Y., Richardson, D.C., Barnouin, O.S., Michel, P., Schwartz, S.R., Ballouz, R.-L., 2018. Rotational failure of rubble-pile bodies: influences of shear and cohesive strengths. Astrophys. J. 857 (1), 15. https://doi.org/10.3847/1538-4357/aab5b2.

Zhao, J., Li, H.B., 2000. Experimental determination of dynamic tensile properties of a granite. Int. J. Rock Mech. Min. Sci. 37, 861–866. https://doi.org/10.1016/s1365-1609(00)00015-0.

Zhou, Z., Li, X., Zou, Y., Jiang, Y., Li, G., 2014. Dynamic brazilian tests of granite under coupled static and dynamic loads. Rock Mech. Rock Eng. 47 (2), 495–505.